Materials Science & Engineering A 819 (2021) 141487

Contents lists available at ScienceDirect

Materials Science & Engineering A

journal homepage: www.elsevier.com/locate/msea

Effect of the heat treatment on the microstructure and hardness evolution of a AlSi10MgCu alloy designed for laser powder bed fusion

A. Martin [a], M. San Sebastian [b], E. Gil [b], C.Y. Wang [c], S. Milenkovic [a], M.T. Pérez-Prado [a], C. M. Cepeda-Jiménez [d,*]

[a] IMDEA Materials Institute, C/ Eric Kandel, 2, 28906, Getafe, Madrid, Spain
[b] LORTEK S. Coop. Technological Centre, Arranomendia 4A, 20240, Ordizia, Spain
[c] State Key Laboratory of Solidification Processing, Northwestern Polytechnical University, 710072, Xi'an, PR China
[d] Department of Physical Metallurgy, Centro Nacional de Investigaciones Metalúrgicas (CENIM-CSIC), Avda, Gregorio del Amo 8, Madrid, 28040, Spain

ARTICLE INFO

Keywords:
Aluminium
Laser powder bed fusion
Additive manufacturing
Microstructure
Precipitation hardening

ABSTRACT

The aim of this work is to investigate the influence of the addition of Cu on the microstructure and on the microhardness of a laser powder bed fusion (L-PBF)-fabricated AlSi10MgCu alloy. With this goal, AlSi10Mg+4 wt%Cu pre-alloyed powder was produced by gas atomization. Following a parameter optimization study, dense as-built specimens with a high relative density of 99.8% were fabricated. An outstanding microhardness value, exceeding 180 HV, was obtained after aging at 160 °C for 16 h. This value is similar to that of the high strength Al 7075 in the T6 condition. With the aid of analytical transmission electron microscopy, it was concluded that the origin of the observed excellent mechanical behavior could be attributed to the beneficial effect of Cu in reducing the Al-matrix cell size, and in increasing the density and decreasing the size of the Si-based nanoprecipitates at cell interiors. More specifically, it is proposed that the maximum hardness is associated to the development of Cu-rich GP-I zones, which act as precursors of Si nanoprecipitates. Overaging leads to a reduction in microhardness due to transformation of these GP-I zones into coarser θ'' precipitates and thus to a smaller volume fraction of larger Si-based nanoparticles.

1. Introduction

Laser powder bed fusion (L-PBF) is an emerging Additive Manufacturing (AM) technique by which successive powder layers are consolidated to make complex geometry parts in a near-net-shape manner [1]. Besides allowing to fabricate components with intricate geometry, L-PBF also constitutes a tool to design and process novel advanced materials, since the high cooling rates involved (10^4–10^7 K/s), which are much faster than the rates associated to conventional processing methods (~10^2 K/s), may give rise to notable changes in the solidified microstructure, including grain refinement, precipitation of out-of-equilibrium phases, increased solid solubility and reduced segregation [2].

However, there are still several technical concerns, involving important scientific challenges, that limit metal L-PBF application. For example, the number of metallic powder feedstock alloys that can be utilized to build defect-free components with high performance is still very limited. Traditional wrought and cast aluminum alloys are not optimized for additive manufacturing and in some cases they may not be printable at all [3]. The physical properties of Al alloys, including a high tendency to oxidation, high thermal conductivity, and large solidification shrinkage, as well as the low flowability and high laser reflectivity of Al powders, are pointed as major hindrances to AM production of these materials [4,5].

To date, the Al12Si and AlSi10Mg aluminum alloys have been the most utilized Al-based L-PBF feedstock because of their good weldability, excellent castability and low shrinkage, resulting from the presence of a large fraction of Al–Si eutectic [6,7]. The high fluidity provided by the large Si content facilitates the production of high-density parts [8,9] whose mechanical performance, however, does not meet the standards required for structural components, as their yield and a maximum strengths are considerably lower than those corresponding to high-strength 7xxx and 2xxx wrought aluminum alloys. Unfortunately, the latter are hardly weldable and thus cannot be utilized to produce defect-free AM parts [8]. Therefore, the development of new aluminum alloys for additive manufacturing with high mechanical

* Corresponding author. Cepeda-Jiménez Department of Physical Metallurgy, CENIM-CSIC, Avda. Gregorio del Amo 8, Madrid, 28040, Spain.
E-mail address: cm.cepeda@cenim.csic.es (C.M. Cepeda-Jiménez).

https://doi.org/10.1016/j.msea.2021.141487
Received 23 March 2021; Received in revised form 21 May 2021; Accepted 22 May 2021
Available online 28 May 2021
0921-5093/© 2021 The Authors. Published by Elsevier B.V. This is an open access article under the CC BY-NC-ND license (http://creativecommons.org/licenses/by-nc-nd/4.0/).

strength appears as particularly desirable and challenging.

Precipitation hardening is one of the most effective mechanisms for improving the mechanical properties of metallic materials [10]. The effectiveness of this strengthening mechanism depends on precipitate characteristics such as the size and shape, the volume fraction, the spatial distribution with respect to the dislocation glide plane, and the mechanism by which dislocations and precipitates interact [11]. As general rule, a high density of incoherent nanometer-sized precipitates would be most effective in blocking mobile dislocations, thus giving rise to the highest strengthening rates [12].

Previous studies [13] have shown Cu addition to increase the strength of foundry Al–Si–Mg alloys, both by its presence in solid solution, as well as by enhancing precipitation hardening. The most common precipitates in Al–Si–Mg cast alloys are β'' and/or β′ phases (precursor of Mg_2Si phases) and θ' (Al_2Cu), S ($CuMgAl_2$) or Q ($Cu_2Mg_8Si_6Al_5$) phases, which may exist in metastable form depending on the processing conditions [14,15]. On the light of these earlier works on cast Al–Si–Mg alloys, it seems reasonable to hypothesize that the addition of Cu to AlSi10Mg alloy powders could also enhance the properties of L-PBF processed parts. Furthermore, it is foreseen that the far from-equilibrium solidification conditions involved in L-PBF may be exploited to enhance precipitation hardening [16,17].

The present work aims to study the influence of the addition of Cu to the AlSi10Mg alloy processed by L-PBF. Pre-alloyed powder, produced by gas atomization, is utilized in order to avoid the problems associated to in-situ powder mixing during the printing process. The influence of Cu addition and the ageing behaviour on the microstructure and Vickers microhardness of the L-PBF-fabricated AlSi10MgCu alloy have been systematically characterized.

2. Experimental procedure

This work investigates the effect of Cu addition on the printability, the microstructure and the hardness of an AlSi10Mg alloy processed by L-PBF. A nominal target Cu amount of 4 wt% was selected, as this quantity lies below the highest solubility limit of Cu in Al. The investigated alloy will be termed hereafter AlSi10Mg–4Cu. Ingots were prepared using high-purity metals (99.9 wt%) by casting in an induction furnace (VSG 002 DS, PVA TePla). Afterwards, pre-alloyed powder was obtained by melting and gas atomization using a LEYBOLD gas atomizer (model VIGA 2S) under argon atmosphere (99.5% purity). The chemical composition of the atomized powder was determined by inductively coupled plasma-optical emission spectrometry (ICP-OES). Powders with sizes between 20 and 63 μm were sieved and selected for subsequent processing by L-PBF. The particle size distribution of the pre-alloyed powder was determined using SEM and with the aid of the ImageJ image analysis software. In addition, the apparent density and the flow characteristics of the powder were evaluated using a Hall funnel following the ASTM B-212-17 and ASTM B-213 standards, respectively.

A parameter optimization study was first carried out with the aim of selecting the L-PBF processing conditions rendering samples with the highest density. AlSi10Mg–4Cu cubes ($10 \times 10 \times 5$ mm^3) were built on top of an inverted pyramidal support to extract them easily from a reduced build volume platform, using a Renishaw AM400 L-PBF system (Renishaw plc, UK) equipped with a pulsed laser. The build plate was preheated at 150 °C. The chamber was prefilled with argon (99.999% purity) in order to minimize oxygen contamination, and thus the O_2 content was measured to be below 500 ppm during the printing process using oxygen sensors within the build chamber. In addition, argon gas flowed across the platform from right to left in order to remove the spattered particles from the powder bed. Layers with a hatch distance (h) of 0.12 mm and a layer thickness (t) of 0.03 mm were scanned using a bidirectional strategy in the scanning plane xy, with z as building direction. Each layer was rotated a fixed angle of 90° with respect to the previous layer in order to homogenize the effect of the laser path. Eight sets of samples were manufactured using two laser power (P) values (275 W and 350 W) and scanning speed values (v) ranging from 1150 to 1600 mm/s. The eight sets of processing conditions, as well as the equivalent volumetric energy density (Ev), are listed in Table 1. Ev has been defined as $Ev=P/vth$, where P is expressed in W, v in mm/s, and t and h in mm. v is given by the equation $v=PD/ET$, where PD (in mm), the point distance, is the distance between the centre of two consecutive melting points, and ET (in s) is the laser exposure time on each point [18]. A PD of 0.08 mm was kept constant in this study. The density of all L-PBF-built samples was determined by optical microscopy (GX51 Olympus) combined with image processing of cross-sectional micrographs using the AnalySIS docu software (Olympus). At least three optical micrographs corresponding to different sections were analyzed in order to improve accuracy. The set of P and v rendering the highest density was thus determined.

Samples processed using the optimum parameter set were aged at 160 °C for 4–20 h and at 180 °C for 2–12 h in a conventional muffle furnace, in order to investigate the influence of the aging conditions on the microstructure and on the microhardness.

The microstructure of the atomized powder and of L-PBF-processed samples was characterized by scanning electron microscopy (SEM), electron backscattered diffraction (EBSD), and transmission electron microscopy (TEM). EBSD examination was performed using a field emission gun (FEG) SEM (Helios NanoLab 600i, FEI) equipped with an HKL EBSD system, a CCD camera, as well as both the Aztec and the Channel 5.0 data acquisition and analysis software packages. EBSD maps were recorded using beam conditions of 15 kV, 2.7 nA, 8 mm working distance and a step size of 0.28 μm. The average grain size was calculated by the linear intercept method from inverse pole figure maps using only GBs with misorientation angles greater than 15°. The precipitate structure was carefully examined by TEM using a Talos F200X FEI operating at 200 kV. TEM characterization was performed both in conventional transmission mode, with a parallel beam, as well as in scanning transmission (STEM) mode, using high angle annular dark field (HAADF) imaging. Elemental mapping was also carried out using energy dispersive X-ray spectroscopy (EDS) in order to investigate the distribution of precipitates and alloying elements both in the atomized powder and in the L-PBF-produced samples before and after annealing treatments. Specimens for TEM observation were prepared by ion milling using a dual-beam SEM-FIB Helios NanoLab 600i, FEI. A trenching-and-lift-out technique, described in great detail in Ref. [19], was adopted to extract lamellae, which were thinned down to approximately 50 nm for electron transparency.

The Vickers microhardness (HV) of the as-built and aged specimens was measured along the building direction with an Emco Test DuraScan microharness tester, using a constant load of 0.5 kg and a dwell time of 10 s, following the standard UNE-EN ISO 6507-1. At least 10 microhardness indents were performed to calculate the average hardness value for each investigated condition.

Table 1
Sets of processing parameters utilized for the optimization of the L-PBF process.

Sample	P (W)	ET (μs)	V (mm/s)	Ev (J/mm^3)
1	275	54	1250	61.1
2	275	49	1350	56.6
3	275	45	1450	52.7
4	275	40	1600	47.7
5	350	60	1150	84.5
6	350	54	1250	77.8
7	350	49	1350	72.0
8	350	45	1450	67.0

P: laser power; ET: Exposure time V: scanning velocity; Ev: volumetric energy density.

3. Results

3.1. Powder characterization

The actual composition of the atomized powder, measured by inductively coupled plasma atomic emission spectroscopy, was Al-10.43 wt% Si-0.31 wt% Mg-5.34 wt% Cu. The average apparent density and the flowability of the powder were 1.53±0.01 g/cm^3 and 76±3 s, respectively. These properties, which control powder spreading and thus have a great influence in the porosity of the printed parts [4], are similar in magnitude to those previously reported for Al alloy powders [20,21].

The morphology, size, and microstructure of the atomized powder were carefully characterized by SEM and TEM (Figs. 1 and 2). Most powder particles exhibit a near-spherical shape with a minor fraction of satellites (Fig. 1a). This morphology is expected to positively affect the process of L-PBF, as it favors efficient powder packing and enhances flowability [20]. As shown in Fig. 1b, the average particle diameter was approximately 52 μm, with D10, D50 and D90 values of 31.8, 52.5, and 68.8 μm, respectively. The SEM micrographs of Fig. 1c and d, that illustrate cross-sections of several particles, show no internal entrapped gas or porosity, which if present could negatively contribute to the formation of cracks or defects. The microstructure of the particles consists of eutectic Al–Si (α-aluminum) cells, approximately 3–5 μm in size (Figs. 1d and 2a). The HAADF-STEM micrograph, and the corresponding elemental map, shown in Fig. 2b and c, respectively, reveal that the intercellular regions are populated by Si- and Cu-based particles that grow adjacent to each other. High resolution TEM imaging of the aluminum matrix (Fig. 2d) confirms the absence of particles at the cell interiors.

3.2. Microstructure of L-PBF-built AlSi10Mg–4Cu specimens

A L-PBF parameter optimization analysis was carried out with the aim of selecting the laser power and scanning velocity values that produced specimens with the highest density. The eight combinations of processing parameters utilized are summarized in Table 1. This processing window was selected as earlier studies [7] determined that low energy density (<50 J/mm^3) leads to high porosity due to insufficient melting, and that energy density values higher than ~80 J/mm^3 produce an increase in the content of defects, such as keyhole pores, due to vaporization. Fig. 3 consists of several optical micrographs illustrating the cross-section of the as-built AlSi10Mg–4Cu cubes printed using the eight different combinations of P and *v*, as well as the corresponding density values. In general, a relatively high density, exceeding 99.55%, was achieved irrespective of the processing conditions. The highest density (99.82%) was obtained using P = 350 W and *v* = 1350 mm/s. Decreasing P and/or increasing *v* resulted on the formation of larger keyhole pores, with irregularly shapes, which originate from the incomplete filling of gaps with molten metal during rapid solidification [22]. At *v* < 1350 mm/s, and P = 350 W, the presence of some round metallurgical pores could be attributed to some degree of instability during the solidification process due to the high *Ev*. Fig. 4 shows that the highest sample densities are in general obtained for *Ev* values ranging from 60 to 75 J/mm^3. This observation agrees with earlier studies [23], which have reported similar optimum *Ev* values in pure Al, and in Al–Si and Al–Mg alloys. In summary, from the present parameter optimization study a laser power of 350 W and a scanning velocity of 1350 mm/s (*Ev* = 72 J/mm^3) were selected.

The microstructure of the as-built AlSi10Mg–4Cu alloy, processed using the selected L-PBF parameter set, was formed by grains elongated along the building direction, as shown in Fig. 5, and with a very weak texture. Figs. 6–8 contain several representative SEM and S/TEM micrographs illustrating the microstructure of these as-built specimens at higher magnification. Fig. 6a reveals, in particular, the presence along the xy plane of arrays of melt pools lying at right angles with respect to each other. The melt pool thickness, measured from *xz* cross-sections (pictures not included), was, on average, approximately 100 μm. Fig. 6b and c (SEM) and 7a (TEM) depict the fine microstructure resulting from L-PBF processing, which is formed by cells with diameters between 400 and 500 nm and with boundaries decorated with particles. It must be noted here that the cell size in the L-PBF processed samples is significantly smaller than that observed in the powder particles (Figs. 1 and 2). This observation is consistent with the presence of higher solidification rates during AM processing than during gas atomization. Fig. 7c confirms the presence of Si- and Cu-rich particles at the intercellular regions. These two types of particles appear to grow adjacent to each other, and no particles containing both Cu and Si are clearly distinguishable. Fig. 8 reveals, additionally, that the cell interiors are populated with numerous nanoscale Al_2O_3 oxides (average size smaller than 10 nm), probably as a consequence of the presence of a small

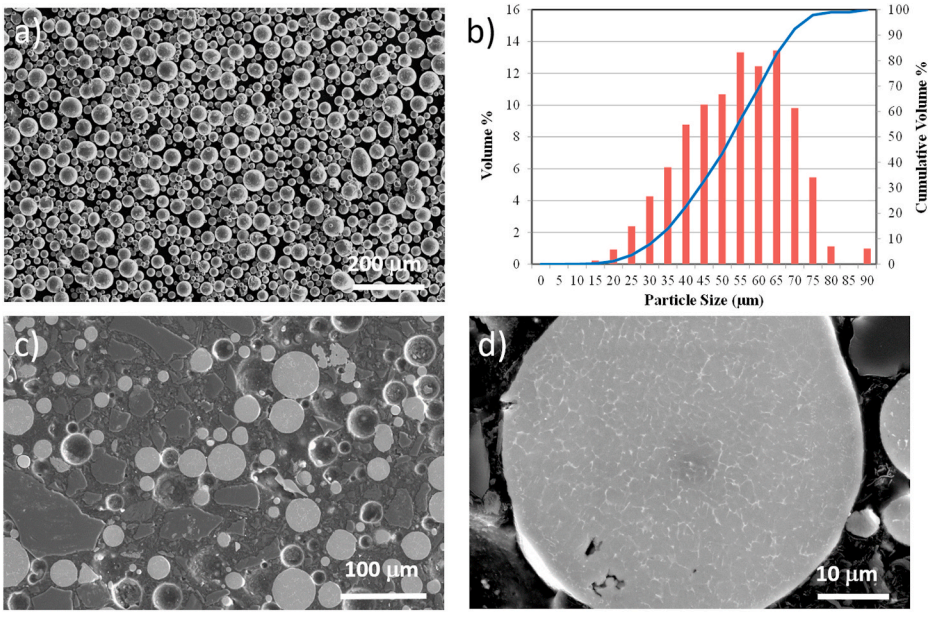

Fig. 1. (a) SEM micrograph illustrating the morphology of AlSi10Mg–4Cu powder particles; (b) particle size distribution; (c,d) SEM imaging of particle cross-sections at different magnifications.

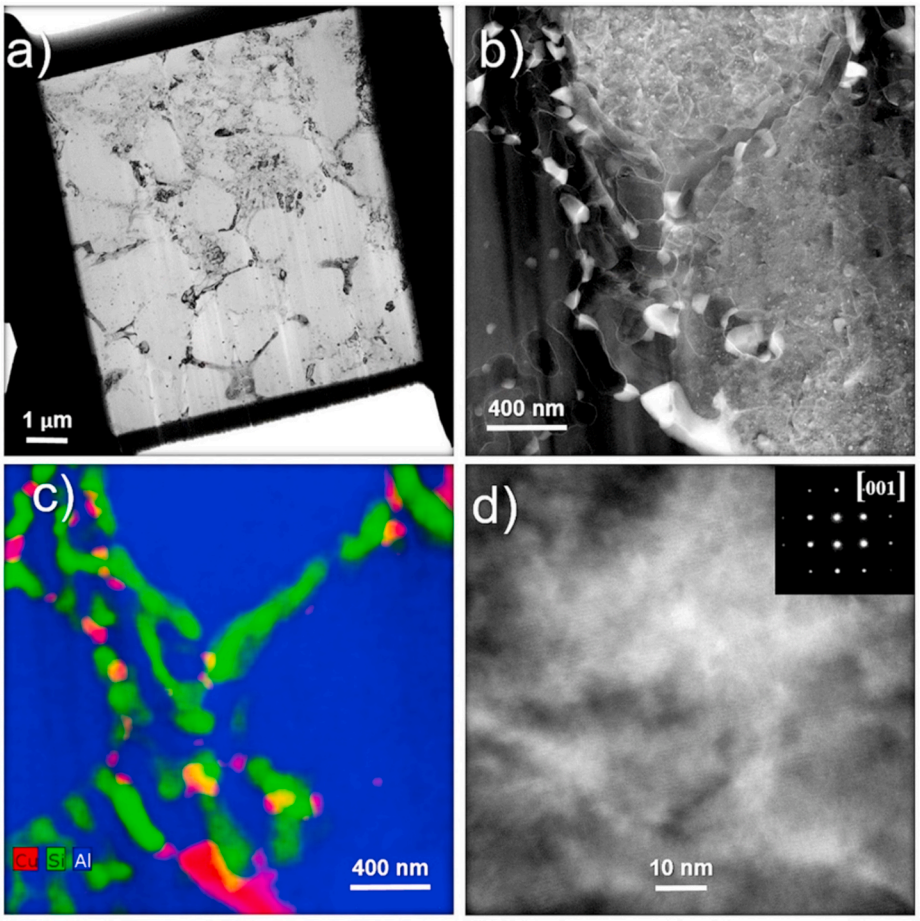

Fig. 2. TEM examination of the microstructure of the AlSi10Mg–4Cu powder particles. (a) Bright field image; (b) HAADF-STEM image; (c) Al, Si, Cu elemental maps corresponding to the area depicted in (b); (d) HRTEM micrograph at high magnification showing absence of precipitates inside the matrix. The zone axis is <001>.

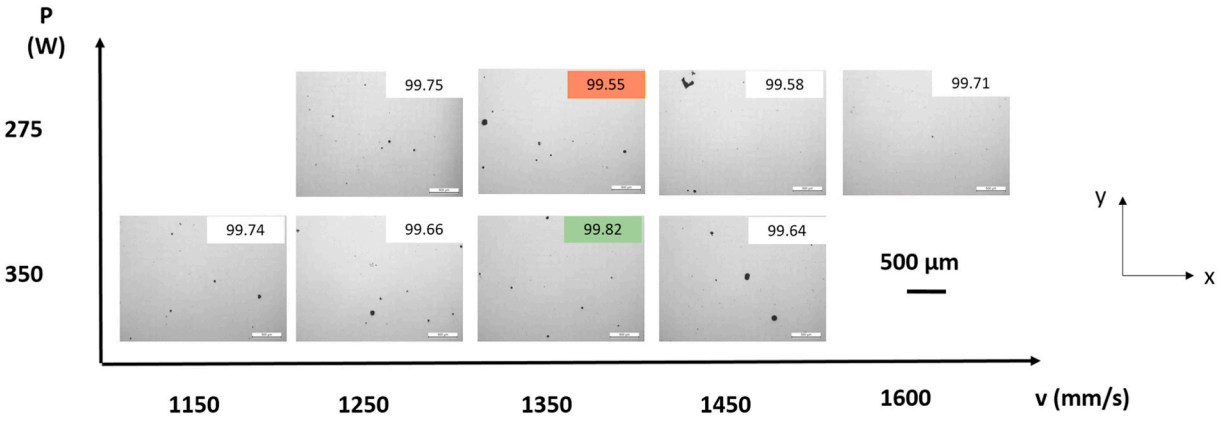

Fig. 3. Optical micrographs illustrating cross sections of the as-built AlSi10Mg–4Cu cubes, obtained using eight combinations of laser power and scanning velocity values, and the corresponding bulk densities.

proportion of oxygen inside the process chamber, as well as with Si, Mg and Cu in solid solution.

3.3. Effect of heat treatments

Selected AlSi10Mg+4Cu samples processed using the selected L-PBF parameters were aged at 160 and 180 °C for different holding times. Fig. 9 depicts the evolution of the Vickers microhardness, measured on the *xz* plane, during aging. While the microhardness of the as-built parts amounts to 156±2 HV, the peak-aged microhardness values are similar to those reported for the high-strength wrought Al 7075 alloy in the T6 condition (175–180 HV) and considerably higher than those reported for the Al 2024-T3 (140–145 HV) [24]. In particular, at 180 °C a maximum microhardness of 175±3 HV is achieved after 4 h, while at 160 °C a maximum microhardness of 183±3 HV is achieved after 16 h.

As exemplified in Fig. 10, which corresponds to a specimen peak-aged at 160 °C for 16 h, aging did not lead to any significant changes in the grain size and in the texture with respect to as-built specimens

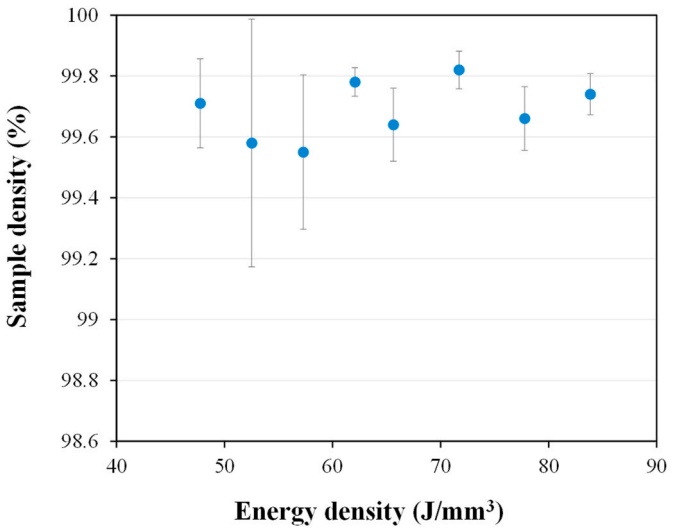

Fig. 4. Density of as-built Al1Si0Mg+4Cu specimens as a function of the energy density.

(Fig. 5). The average grain size, measured by the linear intercept method along the *x* and *z* directions from the corresponding EBSD maps was 3.0 ± 2.6 μm and 4.4 ± 4.2 μm, respectively, for the as-built condition, and 3.0 ± 2.8 μm and 4.7 ± 6.8 μm for the heat treated. This agrees with earlier studies [25,26], which have shown that the grain size and the texture of L-PBF-processed Al–Si alloys remain unchanged even after annealing at 530 °C for 6 h, probably due to the pinning effect exerted by the intercellular eutectic Si phase. Our study revealed additionally, that aging did not change the as-built cellular structure. Fig. 11 contains several bright field TEM micrographs showing the cell structure corresponding to samples aged at 160 °C for 16 h (Figs. 11a), 180 °C for 4 h (Figs. 11b), and 180 °C for 12 h (Fig. 11c). In all cases, the cell size remains approximately equal to 400–500 nm, as in the as-built specimens (Fig. 7a).

The precipitate distribution, however, changed significantly with the heat treatment conditions. Figs. 12–15 present an exhaustive TEM characterization of these precipitates after peak-aging at 160 °C for 16 h (183 HV) (Figs. 12 and 13), as well as after peak-aging at 180 °C for 4 h (175 HV) (Fig. 14) and following overaging at 180 °C for 12 h (167 HV) (Fig. 15). All the images have been taken along <100> directions of the Al matrix. After aging at 160 °C for 16 h the cell interiors become populated with a homogeneous distribution of fine Si-based nanoprecipitates (Fig. 12), in the form of plates parallel to {001} planes and approximately ~5 nm in thickness and ~10–15 nm in length. These nanoprecipitates consume the solute Si in the α-Al matrix and are also present in L-PBF-produced AlSi10Mg after heat treatments [27]. In addition, as shown in Fig. 13, a dispersion of extremely fine rod-like precipitates, approximately 5 nm in length and only one atomic layer in thickness, which in general lie parallel to <001> directions of the Al matrix, are observed to nucleate in the vicinity of the nano-sized Si precipitates. These very fine precipitates have been identified as Cu-rich GP-I zones by EDX analysis (Fig. 13f) [28]. A similar nanoprecipitate distribution, albeit with slightly larger nanoparticles, was observed in the sample aged at 180 °C for 4 h (Fig. 14). In this specimen, the plate-shaped Si nanoprecipitates have an average diameter of ~20–30 nm and the monoatomic Cu-rich layers (GP-I zones), which again tend to precipitate close to Si nanoparticles, are about 10–20 nm in length. In the overaged condition (180 °C for 12 h, Fig. 15) the density of the nanosized Si precipitates is significantly smaller than in the condition that gave rise to the maximum microhardness values (Figs. 12 and 13)

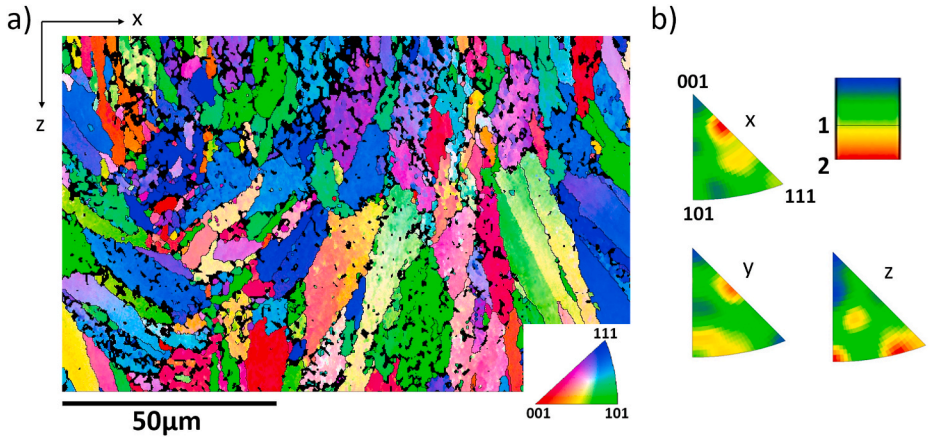

Fig. 5. Microstructure of the as-built AlSi10Mg+4Cu alloy. (a) EBSD IPF map taken along the xz plane and illustrating the orientation of the building direction, where high angle boundaries (θ > 15°) are colored in black; (b) inverse pole figures.

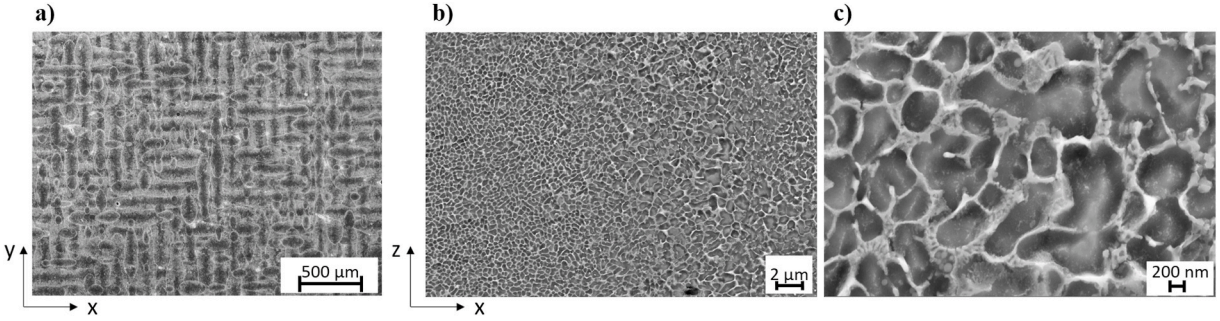

Fig. 6. SEM micrographs illustrating the microstructure of as-built AlSi10Mg+4Cu specimens along the (a) xy and (b,c) xz planes.

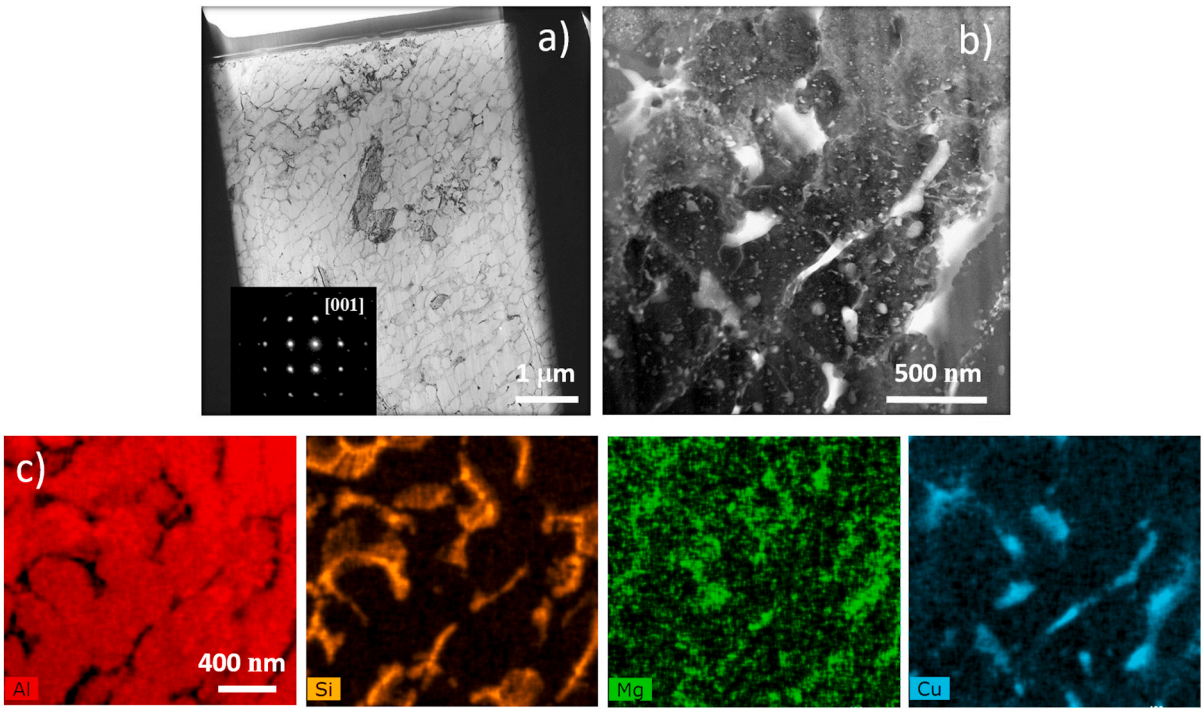

Fig. 7. TEM examination of the microstructure of the as-built AlSi10Mg–4Cu alloy. (a) Bright field image; (b) HAADF-STEM image; (c) Al, Si, Mg, and Cu elemental maps corresponding to the area depicted in (b).

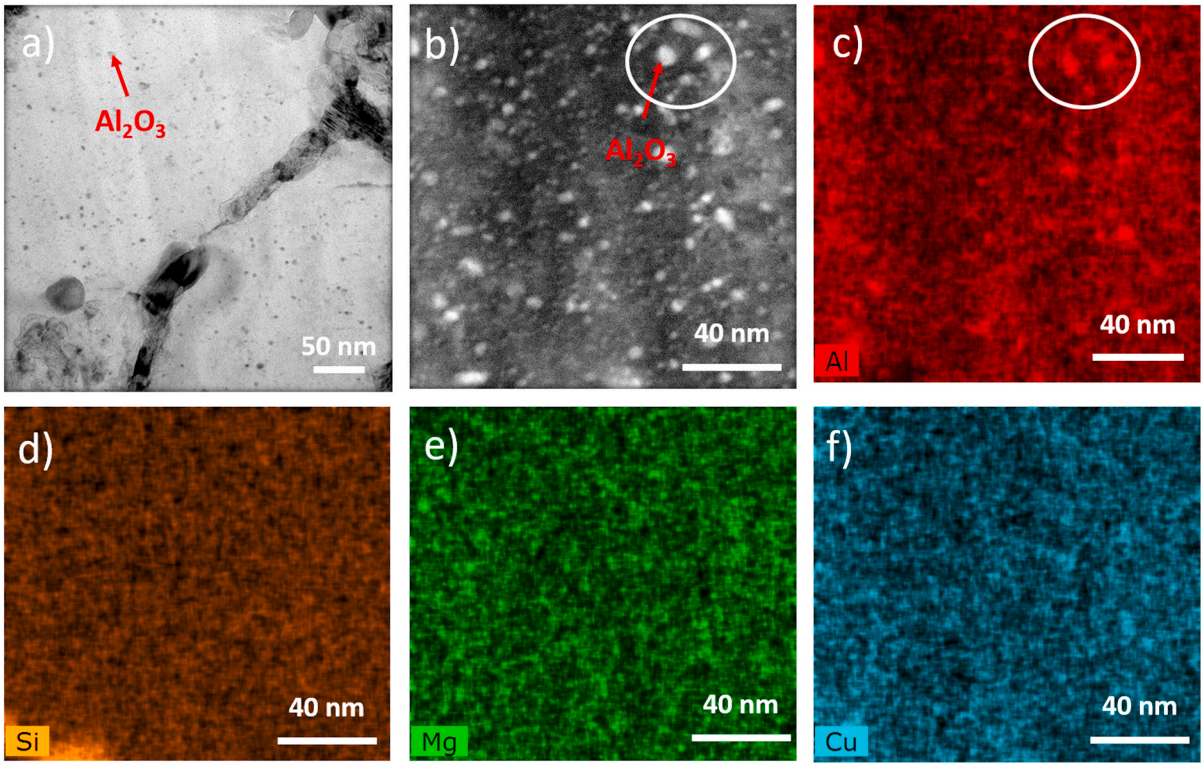

Fig. 8. TEM examination of the microstructure of the as-built AlSi10Mg–4Cu alloy. (a) Bright field image; (b) HAADF-STEM image; (c–f) Al, Si, Mg, and Cu elemental maps corresponding to the area depicted in (b).

and the diameter of the Si nanoparticles increases to about 40–50 nm. In addition, a large fraction of coarser disk shape precipitates, lying parallel to the <001> direction of the Al matrix and with an average length of around 60 nm, can also be observed. The precipitation sequence in the Al–Cu alloy is GP-I (monoatomic Cu layer)>GP-II (two monoatomic Cu layers separated by 3 Al layers)> θ'' (Al_3Cu) (Cu and Al multilayers)> semi-coherent θ' > incoherent θ phase (Al_2Cu) [28]. The Cu precipitates observed in the overaged condition, highlighted with arrows in Fig. 15d

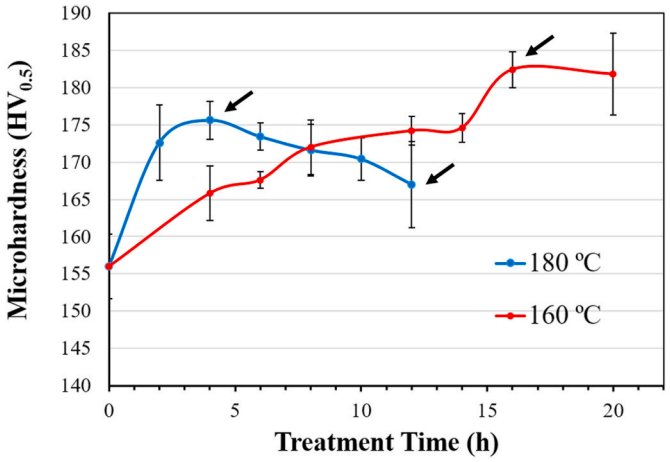

Fig. 9. Vickers microhardness (0.5 kg, 15 s) vs. treatment time corresponding to the as-built AlSi10Mg+4Cu alloy after aging at 160 and 180 °C.

and e, were identified as θ'' (Al_3Cu) [28,29], as they are observed to be coherent with the matrix and to contain several atomic layers. It is noteworthy that, systematically, all the Cu-rich precipitates were found to lie adjacent to the Si-rich particles.

4. Discussion

4.1. Effect of rapid solidification

The rapid solidification conditions inherent to the L-PBF process give rise to distinct microstructural characteristics in the investigated alloy. First, the as-processed AlSi10Mg+4Cu samples possess a high intracellular dislocation density, as shown in the bright-field TEM micrographs displayed in Fig. 16a and b. This high dislocation density can be attributed as well as to the mismatch of thermal expansion coefficients of the Al matrix and of the Si-based crystals in the eutectic region [30,31]. Second, it can also be observed in Fig. 16b and c that the Si-based particles are populated with lamellar nanotwins which, according to earlier studies, can only be found under rapid solidification conditions [32]. Third, our research confirms the presence of a supersaturated solid solution of Si and Cu atoms in the α-Al matrix of the as-built samples. It is well known [33,34] that the solubility of Si in the Al lattice, which is 1.65 wt% at the eutectic temperature, is extended in L-PBF Al–Si alloys to 7 wt%. A higher Cu solubility limit has been also reported for a rapidly solidified AA2024 alloy [35]. In fact, the anomalously high strength of Al–Si based alloys fabricated by selective laser melting (SLM) has been often attributed to the development of a supersaturated solid solution of the α-Al phase [25]. Finally, rapid solidification also contributes to accelerate precipitation. Note that the range of aging temperatures (160-180 °C) considered in this study leads to the peak-aged condition in Al–Cu alloys [29]. Under equilibrium conditions, as those prevalent during conventional casting of Al–Cu alloys [29], the multilayer θ'' (Al_3Cu) precipitates form only after 120 h of aging at 180 °C while in the

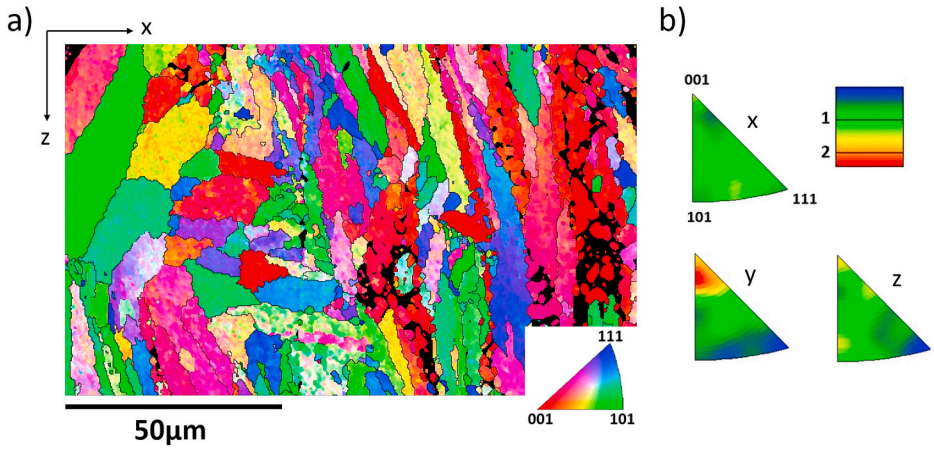

Fig. 10. Microstructure of the AlSi10Mg+4Cu alloy, processed by L-PBF and then peak-aged at 160 °C for 16 h. (a) EBSD IPF map taken along the xz plane and illustrating the orientation of the building direction, where high angle boundaries (θ > 15°) are colored in black; (b) inverse pole figures.

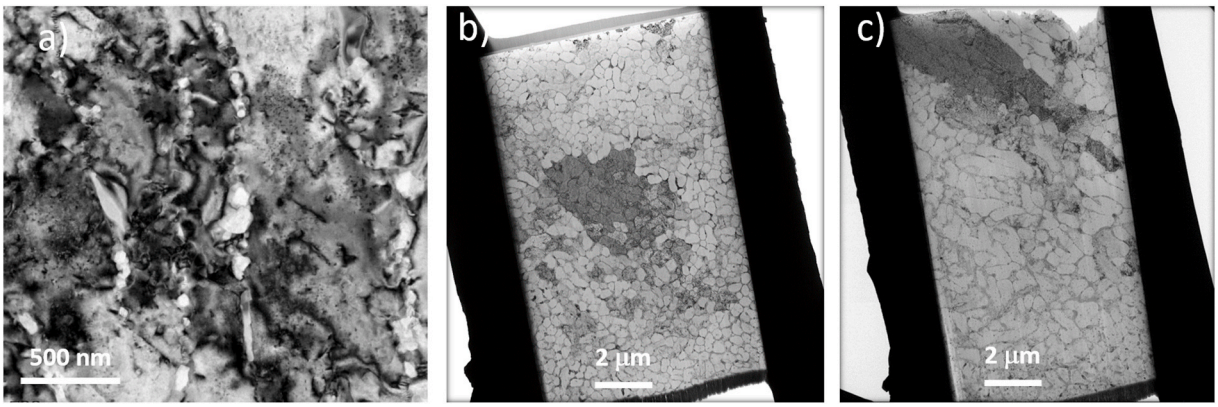

Fig. 11. TEM micrographs illustrating the cell structure corresponding to samples aged at (a) 160 °C for 16 h; (b) 180 °C for 4 h; (c) 180 °C for 12 h.

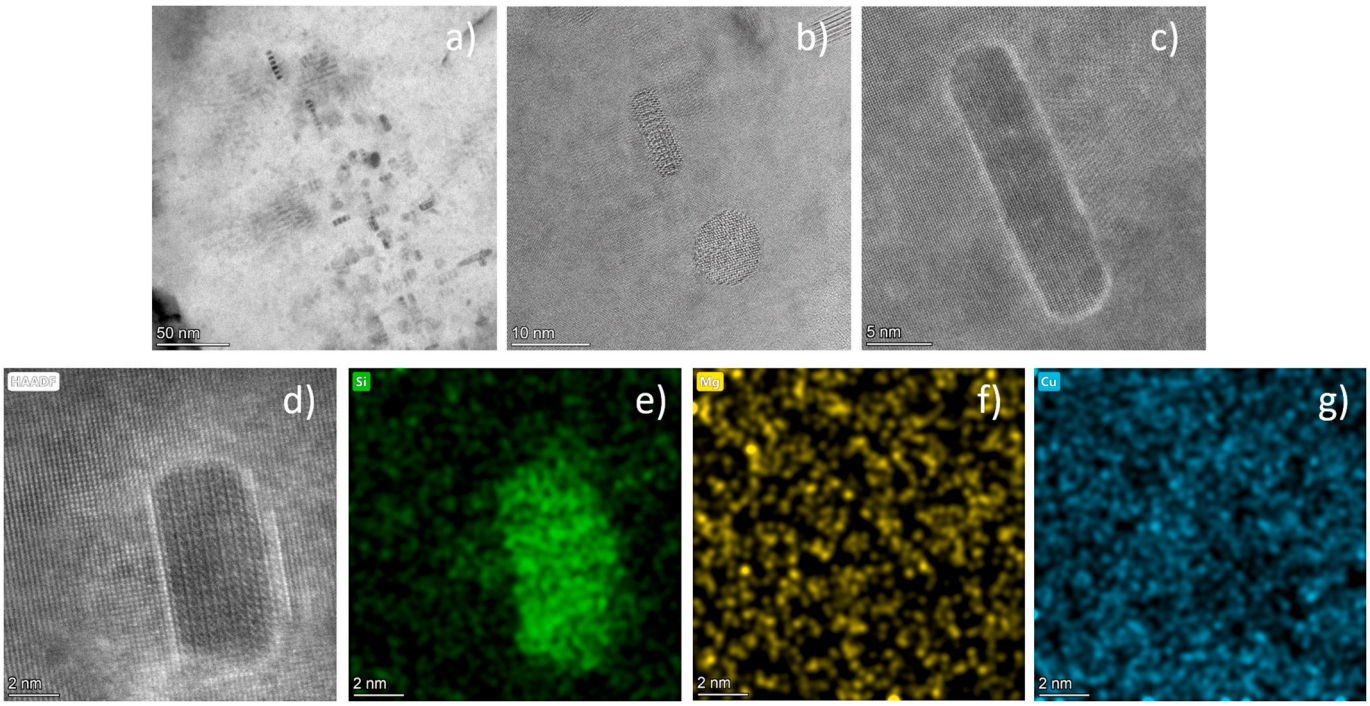

Fig. 12. Precipitation in the AlSi10Mg+4Cu alloy following peak-aging at 160 °C for 16 h (183 HV). (a) Bright field TEM showing a general view of the grain interior; (b–c) HRTEM micrographs of selected plate-shaped particles; (d) HAADF-STEM image of a plate-shaped particle; (e–g) Si, Mg, and Cu elemental maps corresponding to the particle shown in (d). The zone axis is <001>.

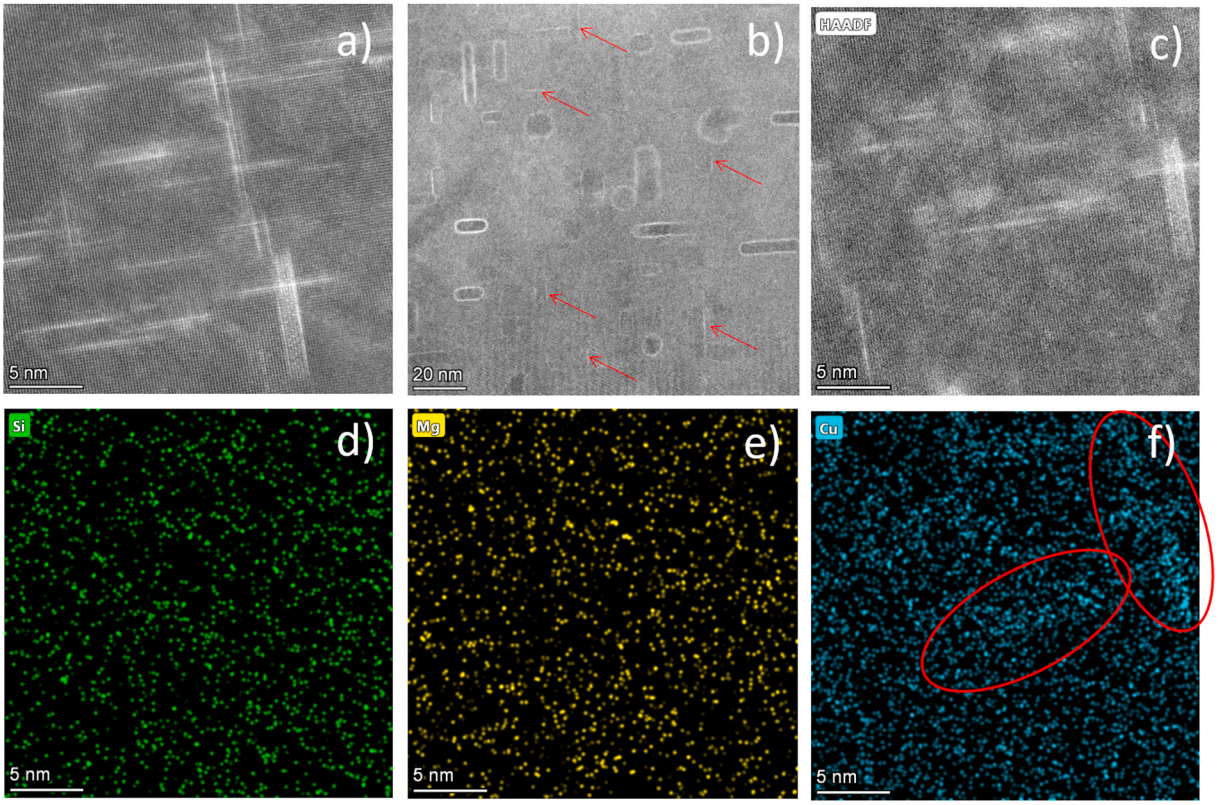

Fig. 13. Precipitation in the AlSi10Mg+4Cu alloy following peak-aging at 160 °C for 16 h (183 HV). (a) HRTEM micrograph illustrating coherent GP zones; b) bright field TEM micrograph illustrating coherent GP zones (red arrows) nucleating in the vicinity of Si-based particles; (c) HAADF-STEM image illustrating coherent GP zones; (d–f) Si, Mg, and Cu elemental maps corresponding to the area depicted in (c). The zone axis is <001>. (For interpretation of the references to color in this figure legend, the reader is referred to the Web version of this article.)

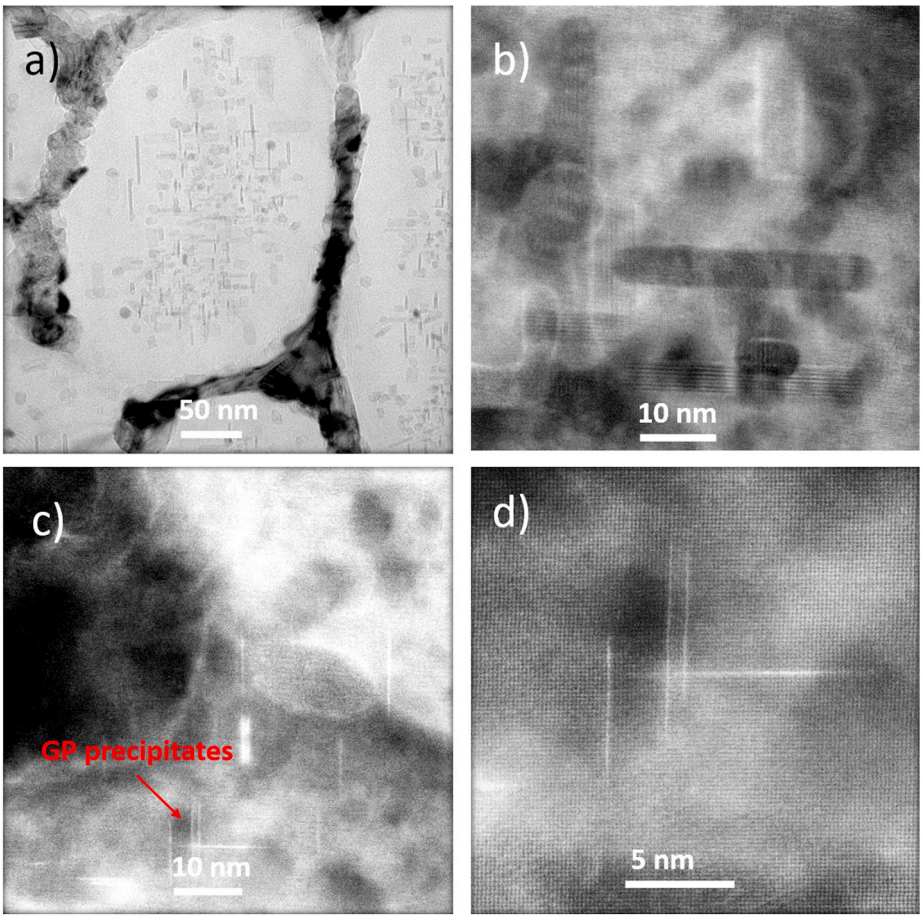

Fig. 14. Precipitation in the AlSi10Mg+4Cu alloy following peak-aging at 180 °C for 4 h (175 HV). (a) Bright field TEM image showing an overview of the precipitate distribution at the cell interiors; (b–d) HRTEM images illustrating a more detailed view of Si-based nanoprecipitates and Cu-based GP zones. The zone axis is <001>.

L-PBF-processed specimens of this study they were observed already after 12 h at this temperature (Fig. 15). It is our contention that the presence of a high dislocation density and of a supersaturated Al matrix phase enable faster diffusion of the elements [36], accelerating the precipitation kinetics during annealing treatments at conventional aging temperatures.

4.2. *Effect of Cu*

The hardness values typical of L-PBF-built AlSi10Mg (without Cu) alloys range from 105 to 133 HV [8]. In general, it has been extensively reported [25,37,38] that these values decrease after aging due to a loss of Si solute in the α-Al matrix. Our results prove that L-PBF-processing and aging of an AlSi10Mg alloy with 4 wt% of Cu leads to microhardness values (175–183 HV) that are comparable to those obtained in structural high strength 7xxx Al alloy series after a T6 hardening treatment (175–180 HV).

In the following, the outstanding hardness values obtained as a result of Cu alloying are rationalized based on the microstructural changes induced by the addition of this element. In order to facilitate this analysis, Fig. 17 illustrates the microstructure of an AlSi10Mg alloy (without Cu), processed by L-PBF using similar processing parameters as those selected for the present study, and aged at the conditions at which the highest hardness values were obtained in the AlSi10Mg–4Cu alloy (160 °C, 16 h), with an average microhardness value 140±6 HV. First, it can be seen that alloying with Cu leads to a reduction of the α-Al cell size, from 1.5 μm (Fig. 17a) to 400–500 nm (Fig. 11). This suggests that the observed Cu solute partitioning to the cell boundaries during AM processing contributes to their refinement. Additionally, Fig. 17 reveals that the size of the Si-rich nanoprecipitates found in the cell interiors after aging in the alloy without Cu ranges from 20 to 100 nm, while the diameter of these nanoparticles was approximately 10–15 nm in the Cu-containing alloy (Fig. 12). The addition of Cu, thus, leads to a reduction of the size and an increase in the density of Si-rich nanoparticles. It is our contention that the precipitation of Cu GP-I zones, observed under peak-aged conditions, favors the precipitation of a high density of nanosized Si-based particles, and that the former contribute to increase the number of nucleation sites. Nucleation of precipitates at GP zones has proved to be an excellent means of obtaining a fine and uniform dispersion of precipitates [39]. This phenomenon has been observed in a number of aluminum alloys, including Al–Zn, Al–Cu, Al–Zn–Mg and Al–Mg–Si. However, since GP zones are coherent, they can be easily sheared by dislocations [40], and thus it is expected that the Cu-rich precipitates would have a minor contribution to the strength of the alloy.

In summary, this research suggests that the outstanding hardness values obtained in the L-PBF-processed AlSi10Mg–4Cu alloy with respect to its Al–Si10Mg counterpart may be explained by the presence of a reduced cell size, a higher density of smaller nanosized precipitates, as well as, to a smaller extent, of shearable Cu-based GP zones.

5. Conclusions

The aim of the present study was to design and characterize a high strength L-PBF-processable Al–Si alloy. With that purpose, 4 wt % of Cu was added to an AlSi10Mg alloy and both the microstructure and the microhardness were evaluated following L-PBF processing and aging at

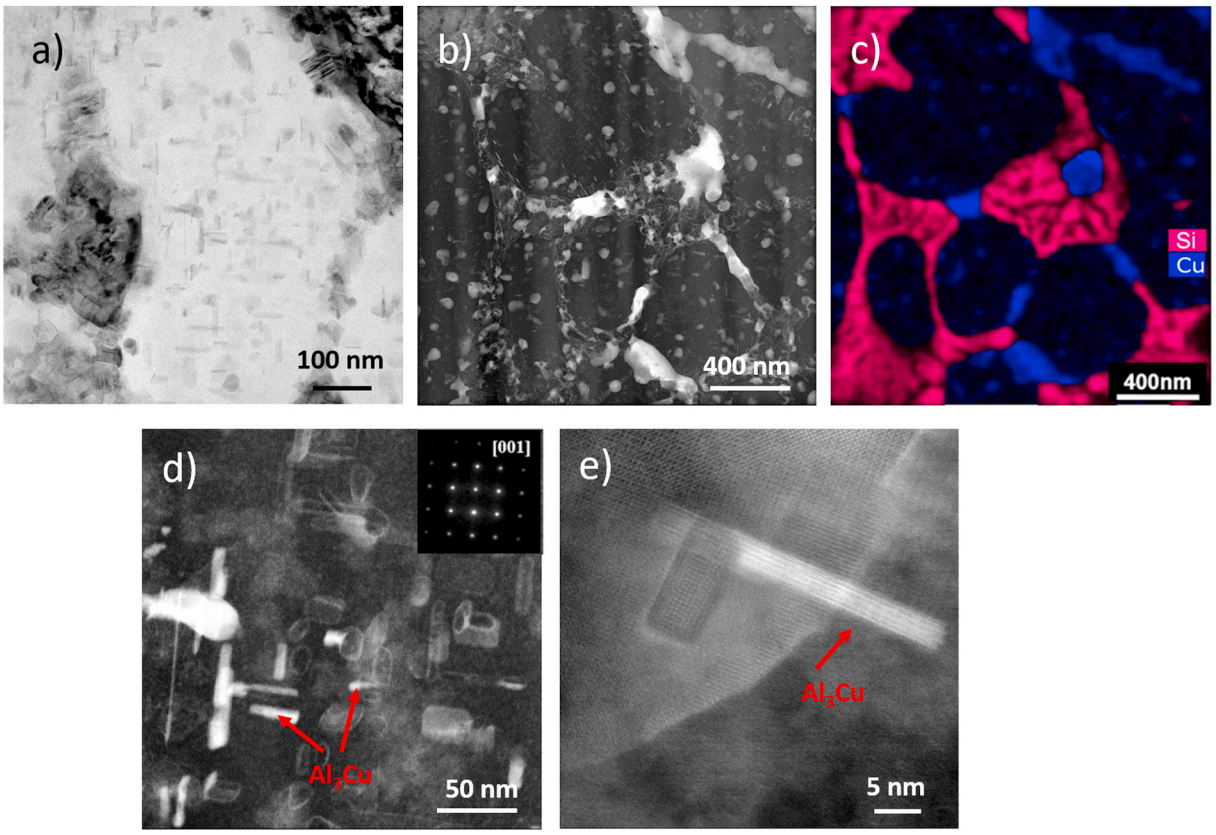

Fig. 15. Precipitation in the AlSi10Mg+4Cu alloy following overaging at 180 °C for 12 h (167 HV). (a) Bright field TEM image showing an overview of the precipitate distribution at the cell interiors; (b) HAADF-STEM image of the precipitate distribution; (c) Si and Cu elemental maps of corresponding to the area depicted in (b); (d) HAADF-STEM image illustrating the presence of Al_3Cu precipitates; (e) HRTEM image of selected precipitates. The zone axis is <001>.

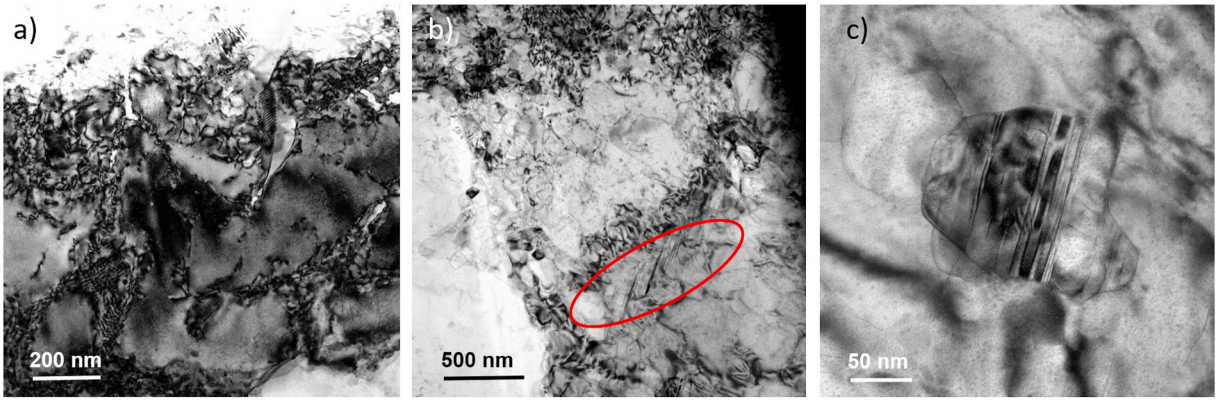

Fig. 16. Bright field TEM micrographs at different magnifications corresponding to the as-built AlSi10Mg+4 wt%Cu sample showing (a,b) a high density of dislocations due to the rapid solidification and (b,c) twinning of the Si-based particles.

different temperatures using a wide range of characterization techniques. The following conclusions may be drawn from this study:

1. A pre-alloyed powder with a nominal composition of AlSi10Mg+4Cu was produced by gas atomization, with a near-spherical shape, flowability and apparent density similar to those previously reported for Al alloy powders. The microstructure of the powder consisted on Al-based cells whose boundaries were populated with Si- and Cu-based particles.
2. Crack-free and dense AlSi10Mg+4Cu samples, with a relative density of 99.82%, were fabricated following a L-PBF parameter optimization process. The resulting microstructure consisted of supersaturated (Si, Cu, Mg) equiaxed α-Al cells (~400–500 nm in size) surrounded by fine eutectic Si and Cu-rich particles, segregated to the intercellular regions.
3. A peak-aged microhardness value comparable to that of the high-strength wrought Al 7075 alloy, in the T6 condition, was obtained in the L-PBF-processed AlSi10Mg+4Cu alloy following aging at 160 °C for 16 h. The outstanding hardness achieved is mainly attributed to the beneficial effect of Cu in, simultaneously, decreasing the cell size and the size of the nanosized Si-based precipitates at cell interiors.

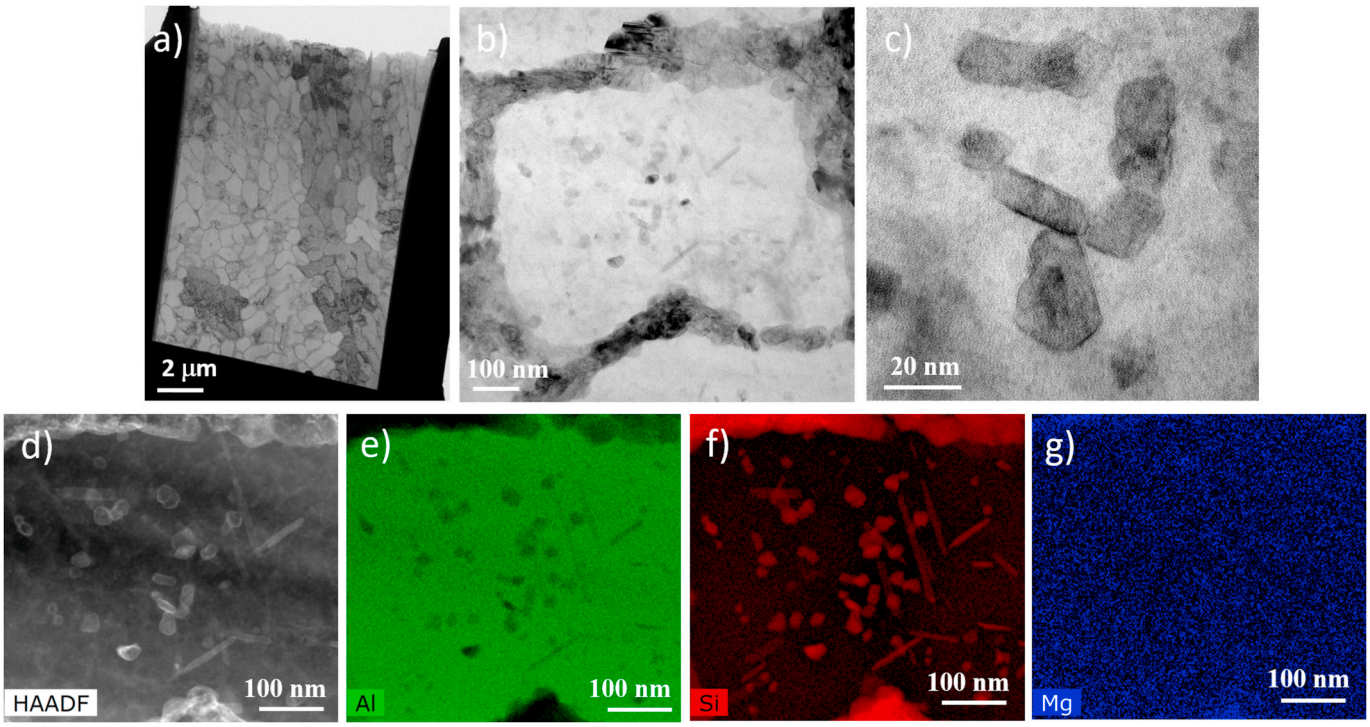

Fig. 17. Microstructure of an AlSi10Mg alloy following L-PBF processing using the selected processing parameters and aged at 160 °C for 16 h (140 HV) (a–c) Bright field TEM micrographs at different magnifications; (d) HAADF-STEM micrograph and (e–g) the corresponding Al, Si, and Mg elemental maps.

4. Cu-based GP zones, which precipitate under peak-aging conditions, appear to act as precursors of nanosized Si-based particles at cell interiors.
5. The results of this study provide new guidelines for the development of AlSi10MgCu alloys for the reliable production of structural components by additive manufacturing under similar processing conditions.

CRediT authorship contribution statement

A. Martin: Investigation, Methodology, Writing – review & editing. **M. San Sebastian:** Conceptualization, Methodology, Resources, Writing – review & editing. **E. Gil:** Investigation, Methodology, Writing – review & editing. **C.Y. Wang:** Investigation, Methodology, Writing – review & editing. **S. Milenkovic:** Conceptualization, Resources, Writing – review & editing. **M.T. Pérez-Prado:** Conceptualization, Writing – original draft, Writing – review & editing. **C.M. Cepeda-Jiménez:** Conceptualization, Methodology, Investigation, Writing – original draft, Writing – review & editing.

Declaration of competing interest

The authors declare that they have no known competing financial interests or personal relationships that could have appeared to influence the work reported in this paper.

Acknowledgments

This work was funded by the European Union's Horizon 2020 Clean Sky 2 research and innovation program under grant agreement No 755610, project AlForAMA. The authors acknowledge the support from the topic manager, Leonardo Aircraft. CYW acknowledges the financial support from the Fundamental Research Funds for the Central Universities in China (grant number 3102019QD0415). MTPP would like to acknowledge funding from the Madrid region under the program S2018/NMT-4381-MAT4.0-CM.

References

[1] A. Yadollahi, N. Shamsaei, Additive manufacturing of fatigue resistant materials: challenges and opportunities, Int. J. Fatig. 98 (2017) 14–31.
[2] J. Abboud, J. Mazumder, Developing of nano sized fibrous eutectic silicon in hypereutectic Al–Si alloy by laser remelting, Sci. Rep. 10 (2020) 12090.
[3] D. Herzog, V. Seyda, E. Wycisk, C. Emmelmann, Additive manufacturing of metals, Acta Mater. 117 (2016) 371–392.
[4] Y. Ding, J.A. Muñiz-Lerma, M. Trask, S. Chou, A. Walker, M. Brochu, Microstructure and mechanical property considerations in additive manufacturing of aluminum alloys, MRS Bull. 41 (2016) 745–751.
[5] X. Fang, L. Zhang, G. Chen, K. Huang, F. Xue, L. Wang, J. Zhao, B. Lu, Microstructure evolution of wire-arc additively manufactured 2319 aluminum alloy with interlayer hammering, Mater. Sci. Eng. A 800 (2021) 140168.
[6] L. Thijs, K. Kempen, J.P. Kruth, J. Van Humbeeck, Fine-structured aluminium products with controllable texture by selective laser melting of pre-alloyed AlSi10Mg powder, Acta Mater. 61 (2013) 1809–1819.
[7] N. Read, W. Wang, K. Essa, M.M. Attallah, Selective laser melting of AlSi10Mg alloy: process optimisation and mechanical properties development, Mater. Des. 65 (2015) 417–424.
[8] A.I. Mertens, J. Delahaye, J. Lecomte-Beckers, Fusion-based additive manufacturing for processing aluminum alloys: state-of-the-art and challenges, Adv. Eng. Mater. (2017) 1700003.
[9] J.C. Hastie, J. Koelblin, M.E. Kartal, M.M. Attallah, R. Martinez, Evolution of internal pores within AlSi10Mg manufactured by laser powder bed fusion under tension: as-built and heat treated conditions, Mater. Des. 204 (2021) 109645.
[10] A.J. Ardell, Precipitation hardening, Metall. Trans. A 16 (1985) 2131–2165.
[11] H. Liu, I. Papadimitriou, F.X. Lin, J. LLorca, Precipitation during high temperature aging of Al Cu alloys: a multiscale analysis based on first principles calculations, Acta Mater. 167 (2019) 121–135.
[12] D.N. Seidman, E.A. Marquis, D.C. Dunand, Precipitation strengthening at ambient and elevated temperatures of heat-treatable Al(Sc) alloys, Acta Mater. 50 (2002) 4021–4035.
[13] Y.J. Li, S. Brusethaug, A. Olsen, Influence of Cu on the mechanical properties and precipitation behavior of AlSi7Mg0.5 alloy during aging treatment, Scripta Mater. 54 (2006) 99–103.
[14] R.X. Li, R.D. Li, Y.H. Zhao, L.Z. He, C.X. Li, H.R. Guan, Z.Q. Hu, Age-hardening behavior of cast Al–Si base alloy, Mater. Lett. 58 (2004) 2096–2101.
[15] G. Wang, Q. Sun, L. Feng, L. Hui, C. Jing, Influence of Cu content on ageing behavior of AlSiMgCu cast alloys, Mater. Des. 28 (2007) 1001–1005.
[16] J.T. McKeown, A.K. Kulovits, C. Liu, K. Zweiacker, B.W. Reed, T. LaGrange, J.M. K. Wiezorek, G.H. Campbell, In situ transmission electron microscopy of crystal growth-mode transitions during rapid solidification of a hypoeutectic Al-Cu alloy, Acta Mater. 65 (2014) 56–68.
[17] G. Li, S.D. Jadhav, A. Martín, M.L. Montero-Sistiaga, J. Soete, M. San Sebastian, C. M. Cepeda-Jiménez, Vanmeensel Kim, Investigation of solidification and

precipitation behavior of Si-modified 7075 aluminum alloy fabricated by laser-based powder bed fusion, Metall. Mater. Trans. 52 (2021) 194–210.
[18] C.M. Cepeda-Jiménez, F. Potenza, E. Magalini, V. Luchin, A. Molinari, M.T. Pérez-Prado, Effect of energy density on the microstructure and texture evolution of Ti-6Al-4V manufactured by laser powder bed fusion, Mater. Char. 163 (2020) 110238.
[19] C.M. Cepeda-Jiménez, M. Castillo-Rodríguez, M.T. Pérez-Prado, Origin of the low precipitation hardening in magnesium alloys, Acta Mater. 165 (2019) 164–176.
[20] N.T. Aboulkhair, N.M. Everitt, I. Ashcroft, C. Tuck, Reducing porosity in AlSi10Mg parts processed by selective laser melting, Additive Manufacturing 1 4 (2014) 77–86.
[21] E.O. Olakanmi, R.F. Cochrane, K.W. Dalgarno, A review on selective laser sintering/melting (SLS/SLM) of aluminium alloy powders: processing, microstructure, and properties, Prog. Mater. Sci. 74 (2015) 401–477.
[22] R. Xiao, X. Zhang, Problems and issues in laser beam welding of aluminum-lithium alloys, J. Manuf. Process. 16 (2014) 166–175.
[23] E.O. Olakanmi, Selective laser sintering/melting (SLS/SLM) of pure Al, Al-Mg and Al-Si powders: effect of processing conditions and powder properties, J. Mater. Process. Technol. 213 (2013) 1387–1405.
[24] C.M. Cepeda-Jiménez, P. Hidalgo, M. Pozuelo, O.A. Ruano, F. Carreño, Influence of constituent materials on the impact toughness and fracture mechanisms of hot-roll-bonded aluminum multilayer laminates, Metall. Mater. Trans. 41 (2010) 61–72.
[25] N. Takata, M. Liu, H. Kodaira, A. Suzuki, M. Kobashi, Anomalous strengthening by supersaturated solid solutions of selectively laser melted Al-Si based alloys, Additive Manufacturing 33 (2020) 101152.
[26] J.G. Santos-Macías, T. Douillard, L. Zhao, E. Maire, G. Pyka, A. Simar, Influence on microstructure, strength and ductility of build platform temperature during laser powder bed fusion of AlSi10Mg, Acta Mater. 201 (2020) 231–243.
[27] L. Zhao, J.G. Santos-Macías, L. Ding, H. Idrissi, A. Simar, Damage mechanisms in selective laser melted AlSi10Mg under as built and different post-treatment conditions, Mater. Sci. Eng. A 764 (2019) 138210.
[28] T. Stegmüller, F. Haider, Multi-scale cluster dynamics modelling of Guinier-Preston zone formation in binary Al-Cu alloys, Acta Mater. 177 (2019) 240–249.
[29] A. Rodríguez-Veiga, B. Bellón, I. Papadimitriou, G. Esteban-Manzanares, I. Sabirov, J. LLorca, A multidisciplinary approach to study precipitation kinetics and hardening in an Al-4Cu (wt. %) alloy, J. Alloys Compd. 757 (2018) 504–519.
[30] X. Ding, L. Wang, Heat transfer and fluid flow of molten pool during selective laser melting of AlSi10Mg powder: simulation and experiment, J. Manuf. Process. 26 (2017) 280–289.
[31] T. Laha, A. Agarwal, T. McKechnie, K. Rea, S. Seal, Synthesis of bulk nanostructured aluminum alloy component through vacuum plasma spray technique, Acta Mater. 53 (2005) 5429–5438.
[32] H.-H. Lien, J. Mazumder, J. Wang, A. Misra, Ultrahigh strength and plasticity in laser rapid solidified Al-Si nanoscale eutectics, Mater. Res. Lett. 8 (2020) 291–298.
[33] X.P. Li, X.J. Wang, M. Saunders, A. Suvorova, L.C. Zhang, Y.J. Liu, M.H. Fang, Z. H. Huang, T.B. Sercombe, A selective laser melting and solution heat treatment refined Al–12Sialloy with a controllable ultrafine eutectic microstructure and 25% tensile ductility, Acta Mater. 95 (2015) 74–82.
[34] N.T. Aboulkhair, I. Maskery, C. Tuck, I. Ashcroft, N.M. Everitt, On the formation of AlSi10Mg single tracks and layers in selectivelaser melting: microstructure and nano-mechanical properties, J. Mater. Process. Technol. 230 (2016) 88–98.
[35] H. Zhang, H. Zhu, T. Qi, Z. Hu, X. Zeng, Selective laser melting of high strength Al-Cu-Mg alloys: processing, microstructure and mechanical properties, Mater. Sci. Eng. A 656 (2016) 47–54.
[36] Z. Feng, Y. Yang, B. Huang, et al., Precipitation process along dislocations in Al-Cu-Mg alloy during artificial aging, Mater. Sci. Eng. A 528 (2) (2010) 706–714.
[37] E. Padovano, C. Badini, A. Pantarelli, F. Gili, F. D'Aiuto, A comparative study of the effects of thermal treatments on AlSi10Mgproduced by laser powder bed fusion, J. Alloys Compd. 831 (2020) 1548222.
[38] M. Giovagnoli, M. Tocci, A. Fortini, M. Merlin, M. Ferroni, A. Migliori, A. Pola, Effect of different heat-treatment routes on the impact properties of an additively manufactured AlSi10Mg alloy, Mater. Sci. Eng., A 802 (2021) 140671.
[39] P.E. Marth, H.I. Aaronson, G.W. Lorimer, T.L. Bartel, K.C. Russell, Application of heterogeneous nucleation theory to precipitate nucleation at GP zones, Metall. Mater. Trans. 7 (1976) 1519–1528.
[40] B. Bellón, S. Haouala, J. LLorca, An analysis of the influence of the precipitate type on the mechanical behavior of Al-Cu alloys by means of micropillar compression tests, Acta Mater. 194 (2020) 207–223.